European Conference on Computational Fluid Dynamics
ECCOMAS CFD 2006
P. Wesseling, E. Oñate and J. Périaux (Eds)

HIGHER ORDER HYPERBOLIC - COUPLED - ELLIPTIC FLUX-CONTINUOUS CVD FINITE VOLUME SCHEMES IN TWO AND THREE DIMENSIONS

Michael G Edwards

Civil and Computational Engineering Centre
School of Engineering
University of Wales Swansea
Singleton Park Swansea SA2 8PP WALES UK
e-mail: M.G.Edwards@swansea.ac.uk

Key words: Higher-Order, Flux-Continuous, Full-tensor, Finite-volume, Unstructured

Abstract. *Novel unstructured grid higher order convection schemes are presented. The schemes are coupled with locally conservative flux continuous control-volume distributed (CVD) finite-volume schemes for the porous medium general tensor pressure equation on structured and unstructured grids in 2-D and 3-D.*

The schemes are developed for multi-phase flow in porous media. Benefits of the schemes in terms of improved front resolution and medium discontinuity resolution are demonstrated. Comparisons with current methods including the control-volume finite element method highlight the advantages of the new formulation for three dimensional reservoir simulation.

1 INTRODUCTION

This paper presents the development of three dimensional higher order convection schemes coupled with optimal discrete continuous Darcy fluxes for approximation of the multi-phase flow equations that arise in reservoir simulation. The system of equations considered here is hyperbolic fluid transport coupled with an elliptic system for pressure and Darcy velocity [1,2].

A novel higher order scheme with local maximum principle for unstructured grids in three dimensions is presented. The higher order convection schemes presented here are based on the hyperbolic schemes presented in [3,19], with improved time accuracy via a weighted Crank-Nicolson formulation[5]. Higher order convection schemes for reservoir simulation have been developed over a number of years, e.g. [3−11,19]. These schemes achieve higher order accuracy and are constructed such that the solution remains free of spurious oscillations. These methods yield benefits in terms of improved front resolution and have been successfully demonstrated for a variety of multi-phase flow problems in subsurface reservoir simulation.

The continuous Darcy flux schemes presented here are a three dimensional generalization of the two-dimensional elliptic schemes presented in [3]. Previous work in the area of locally conservative flux-continuous full-tensor finite-volume schemes includes [12–26,39–41]. These schemes are control-volume distributed CVD where flow variables and rock properties are associated with the control-volumes of the grid and provide a consistent discretization of the porous medium pressure equation applicable to general geometry and permeability tensors on structured and unstructured grids e.g. [12]. Methods of this type are also known as Multi-point Flux approximation schemes (MPFA) [20]. Mixed finite element methods (MFEM) e.g. [7,27–31] preserve flux continuity for full tensor flows, however mixed methods solve for velocity components and pressure in a globally coupled system. For a three dimensional structured grid MFEM involve solving for 4 times as many degrees of freedom as (the more efficient) CVD methods. The CVD schemes presented here maintain flux continuity with one discrete pressure value per control-volume.

Coupling of the novel higher order phase component approximations with the general tensor flux-continuous formalism is a new development for general grids in three dimensions. Here *general* is used in the sense of allowing the grid to be composed of any element type, arbitrary distortions of such grids and their effects remain to be investigated. The new formulation yields an improved scheme for reservoir simulation applicable to multiphase flow while using an optimal number of degrees of freedom within the discretization.

Flow equations are presented in section 2. A brief summary of the three dimensional flux-continuous CVD formulation is presented in section 3. Extension of the higher order spatial schemes to general unstructured grids is presented in section 4 together with improved temporal accuracy. Two-phase flow results are presented in section 5 that demonstrate the advantages of the new higher order flux-continuous formulation in terms of grid orientation and front resolution. Comparisons with the standard control-volume finite element CVFE scheme [32], (exactly the same number of degrees of freedom), demonstrate advantages of the new formulation with respect to medium discontinuity resolution for reservoir simulation. Conclusions are presented in section 6.

2 FLOW EQUATIONS

The flow equations are briefly described here, the reader is referred to [1] for a comprehensive account. The schemes presented here are illustrated with respect to two phase incompressible flow models, where without loss of generality unit porosity is assumed and capillary pressure and dispersion are neglected. The integral form of the flow equations is given over a control volume Ω_{cv} with surface $\partial\Omega_{cv}$, the continuity equations for phases $p = 1, N_p$ are written as

$$\int_{\Omega_{cv}} (\frac{\partial S_p}{\partial t} + \nabla \bullet \mathbf{V}_p) \mathrm{d}\tau = m_p \tag{1}$$

where S_p, $\mathbf{V}_p$ and m_p are the *pth* phase saturation, Darcy velocity (defined below) and

specified phase flow rate respectively and phase saturations sum to unity.
The momentum equations are defined through Darcys law where the p^{th} phase velocity is defined by

$$\mathbf{V}_p = \mathrm{f}_p(\mathbf{V}_T - \triangle\rho(\mathbf{S})g\mathbf{K}\nabla h) \tag{2}$$

here f_p is the fractional flow of phase p, and $\mathbf{V}_T$ is the total Darcy velocity defined via

$$\mathbf{V}_T = -\Lambda\mathbf{K}(\nabla\phi + \bar{\rho}g\nabla h) \tag{3}$$

where Λ is the total mobility [1], $\mathbf{K}$ is a diagonal or full elliptic Cartesian permeability tensor, ϕ is the pressure and $\nabla = \partial_{x_i}$.

Also, $\bar{\rho} = \sum_{p=1}^{N_p} \rho_p\lambda_p/\Lambda$ is the mean density and λ_p, ρ_p are the p^{th} phase mobility and density respectively, $\triangle\rho(\mathbf{S}) = (\rho_p - \bar{\rho})$, h is the height, g the acceleration due to gravity.

The closed surface integral of phase velocity can now be expressed as the sum of outward normal phase fluxes F_{p_i} over each of the surface increments of the control-volume Ω_{cv}, viz

$$\oint_{\partial\Omega_{cv}} \mathbf{V}_p \bullet \hat{\mathbf{n}}\mathrm{d}s = \sum_{i=1}^{N_S} \mathrm{F}_{p_i} \tag{4}$$

where N_S is the number of surface increments that enclose the volume Ω_{cv}. The outward normal phase flux in the i^{th} normal direction is written in terms of the general tensor $\mathbf{T}$ as

$$\mathrm{F}_{p_i} = -\int_{\partial\Omega_{cv}} \mathrm{f}_p\Lambda(\sum_{j=1}^{3} T_{ij}\phi_{\xi_j} + \rho_p g\sum_{j=1}^{3} T_{ij}h_{\xi_j})\mathrm{d}\Gamma_i \tag{5}$$

where ξ_i are local curvilinear parametric coordinates, Γ_i is the parametric coordinate surface increment and ϕ_{ξ_j} is the derivative of ϕ with respect to ξ_j and

$$\mathbf{T} = J\mathbf{J}^{-1}\mathbf{K}\mathbf{J}^{-T} \tag{6}$$

is the general tensor defined via the Piola transformation which is function of the Cartesian permeability tensor and geometry, where $J_{ij} = \partial x_i/\partial\xi_j$ is the Jacobian of the local curvilinear coordinate transformation. General full tensors can arise (with non-zero cross terms $T_{ij} \neq 0$ for $i \neq j$) as a result of the grid type, local orientation of the grid and permeability field and from upscaling. For incompressible flow Eq. 1 is summed over the N_p phases and since saturations sum to unity, using Eq's. 4, 5 the pressure equation

$$\sum_{i=1}^{N_S} \mathrm{F}_{T_i} = M \tag{7}$$

is obtained. In order to simplify notation gravity will now be omitted from the formalism, however once the discrete flux is defined gravity can be included by following the above definitions. Now using

$$\mathrm{F}_{p_i} = -\int_{\partial\Omega_{cv}} \mathrm{f}_p \Lambda \sum_{j=1}^{3} T_{ij}\phi_{\xi_j} \mathrm{d}\Gamma_i \tag{8}$$

the total flux is given by

$$\mathrm{F}_{T_i} = -\int_{\partial\Omega_{cv}} \Lambda \sum_{j=1}^{3} T_{ij}\phi_{\xi_j} \mathrm{d}\Gamma_i \tag{9}$$

and involves a product of total mobility and single phase flux. Note that the single phase flux is obtained by setting $\Lambda = 1$ in Eq. 9. Zero normal flux (Neumann) applies on solid walls, here M is the total inflow/outflow flux which is zero away from wells. Initial data in terms of saturation and pressure fields are also prescribed. Further details can be found in [1].

3 FLUX-CONTINUOUS CONTROL-VOLUME DISTRIBUTED (CVD) APPROXIMATIONS in 3-D

The initial or primal grid is comprised of cells, with corners defined by the grid vertices. The distinction between cell centred and cell vertex schemes is discussed in [3]. The schemes presented here are vertex centred, where for a given control-volume surrounding a grid vertex, flow variables are assigned to grid vertices *and* rock properties are piecewise constant with respect to the control-volumes and are control-volume distributed CVD. The physical constraints that must be enforced are continuity of pressure and continuity of normal flux across interfaces (control-volume faces) that separate changes in permeability tensor.

3.1 *Continuous Flux Approximation in Three Dimensions*

We now consider approximation of the incompressible single phase flow pressure equation and present a summary of the flux-continuous formulation in three dimensions. Previous work on flux-continuous schemes in 3-D is presented in [15,21,24,26]. The primal grid considered here can be a hybrid composed of combinations of tetrahedra, prisms, pyramids and hexahedra elements in 3-D. In principle the only restriction on grid structure is that tetrahedra can only be joined to hexahedra through a pyramid interface. A polyhedral control-volume is built around each grid vertex, generating a primal-dual grid. Starting in a primal grid cell, the cell centre is joined to cell face mid-points, cell face mid-points are joined to cell edge mid-points. As a result the primal grid cells are decomposed into sub-hexahedra or subcells, four for a tetrahedra, five for a pyramid, six for a prism and eight for a hexahedra. In each case the number of subcells corresponds to the number

of vertices defining the primal cell, and each subcell belongs to the control-volume of the unique vertex to which it is attached. Cell vertex control-volumes are defined by a local assembly or recomposition at each primal grid vertex of all subcells that are attached to the vertex. The resulting set of polyhedral control-volumes defines a dual grid relative to the primal grid which we call the primal-dual. Rock permeability and porosity are assumed to be piece-wise constant over each polyhedral control-volume and flow variables belong to the control-volumes and are vertex centred. Fig's. 1 and 2. Therefore discontinuities in rock properties occur over the control-volume faces.

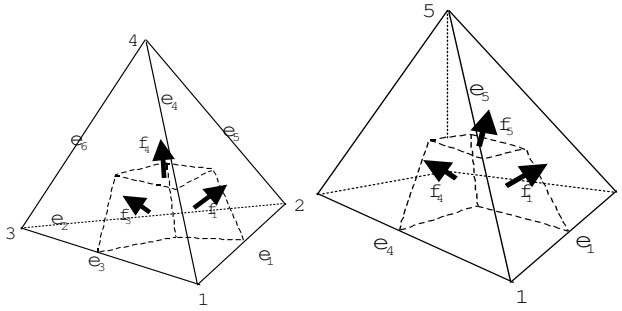

(a) (b)

Figure 1: Subcell (dashed line) of the control-volume surrounding primal cell vertex local number 1, for (a) Tetrahedra (b) Pyramid

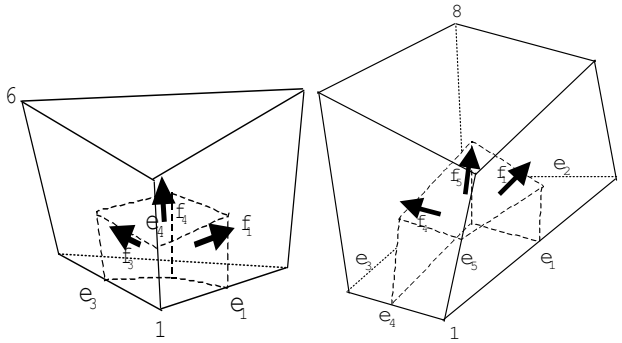

(a) (b)

Figure 2: Subcell (dashed line) of the control-volume surrounding primal cell vertex local number 1, for (a) Prism (b) Hexahedra

As with all finite volume schemes we begin with application of the Gauss divergence theorem to the integral of divergence c.f. Eq. (1) over a given control-volume. A unique discrete flux is then constructed for each control-volume face and the closed integral of

flux is approximated by the sum of discrete outward normal fluxes. For a given face between two neighbouring control-volumes, the unique flux is subtracted from the left hand control-volume and added to the right hand control-volume leading to a locally conservative scheme with respect to the faces of the polyhedral control volumes that contain the discrete permeability tensors with flow variables defined at their vertices.

The finite volume schemes presented here are also designed to be *continuous* across the control-volume faces over which permeability is discontinuous. This is an important distinction between this formulation and other standard formulations such as CVFE. While a flux continuous scheme is locally conservative, the converse is not necessarily true.

Within the flux build process, fluxes are approximated on control-volume subcell faces inside each primal grid cell, in analogous steps to 2-D [3]. Flux continuity conditions are discussed in the next subsection. Each subcell flux is associated with a unique cell edge, the number of (primal-cell) fluxes constructed inside each primal cell is equal to the number of edges, 12 for a hexahedra, 9 for a prism, 8 for a pyramid and 6 for a tetrahedra.

The subcell fluxes are accumulated with respect to their primal cell edges within an assembly process. The edge index $e(i,j)$ refers to the j^{th} primal edge attached to vertex i. The net edge based single phase flux $F_{e(i,j)}(\phi)$ associated with edge $e(i,j)$ is comprised of the sum of adjacent sub-cell fluxes that belong to the primal grid cells with common edge $e(i,j)$, with

$$F_{e(i,j)}(\phi) = \sum_{\sigma=1}^{N_{SCE}} F_{\sigma}(\phi) \tag{10}$$

where N_{SCE} is the number of subcells attached to the edge $e(i,j)$. After assembly of net edge based fluxes, the discrete scheme for each vertex i is completed with the closed integral of net Gaussian flux approximated by the sum of net edge based fluxes connected to the ith vertex. For single phase flow on unstructured grids the assembled finite volume scheme at vertex i can be written concisely as

$$\sum_{j=1}^{N_{edV}} F_{e(i,j)}(\phi) = M_i \tag{11}$$

where summation is over all N_{edV} edges passing through the i^{th} grid vertex, (M_i denotes a specified flow rate at vertex i, or is zero otherwise).

3.2 *Control-Volume Flux and Continuity*

Here a summary of the continuous algebraic flux approximation is given. A consistent normal flux approximation is constructed such that pressure and normal flux are continuous across control-volume faces inside a primal grid cell. In order to achieve this (as in 2-D [3]) local interface pressures are introduced, one per control-volume sub-face, establishing

point-wise continuity in pressure. Sub-cell tetrahedral basis functions are then formed by joining the cell vertices (with locally numbered vertex pressures $\mathbf{\Phi}_v$) to the positions of the adjacent interface pressures $\mathbf{\Phi}_f$ and three normal fluxes are defined with respect to each subcell, on the three faces of each subcell that are inside the primal grid cell, except for the pyramid summit[42]. Flux continuity is then imposed by equating fluxes on the left and right hand sides (L, R) of each of the interfaces in each primal cell resulting in

$$F_i = -\beta(T_{i1}\phi_\xi + T_{i2}\phi_\eta + T_{i3}\phi_\zeta)|_\sigma^L = -\beta(T_{i1}\phi_\xi + T_{i2}\phi_\eta + T_{i3}\phi_\zeta)|_\sigma^R \tag{12}$$

for each interface. Here $\beta = 1/n_f$ where n_f is the number of subcell faces making one interior surface that slices through a primal cell, e.g. for a hexahedra $n_f = 4$. The general tensor $\mathbf{T}$ of Eq. (6) is approximated locally by resolving full-tensor fluxes with respect to the sub-cell geometry and control-volume permeability. The flux continuity equations Eq.12 define a local system of equations for the interface pressures, where the number of continuity equations matches the number of interface pressures and is equal to the number of edges of the primal cell. The discrete pressure field has a piecewise linear variation over each subcell tetrahedra and consequently approximations of the derivatives ϕ_ξ, ϕ_η and ϕ_ζ are linear functions of $\mathbf{\Phi}_f$ and $\mathbf{\Phi}_v$. Here $\Gamma\ |_\sigma^j$ denotes interface flux Γ at location σ and state of volume j. The actual position of σ on each sub-cell face defines both the point of continuous pressure and the flux quadrature, and in turn leads to a family of schemes analogous to [18]. In this paper tests with flux continuity quadrature points correspond to the base members of the families of schemes with quadrature $q = 1$, as defined in [12,18]. A summary of pyramid discretization is given in[42].

The algebraic system of fluxes of Eq. (12) are rearranged in the form

$$\mathbf{F} = A_L\mathbf{\Phi}_f + B_L\mathbf{\Phi}_v = A_R\mathbf{\Phi}_f + B_R\mathbf{\Phi}_v \tag{13}$$

and thus the interface pressures can be expressed *locally* in terms of the cell vertex pressures. After elimination of the Φ_f from Eq. (13) it follows that

$$\mathbf{F} = (A_L(A_L - A_R)^{-1}(B_R - B_L) + B_L)\mathbf{\Phi}_v \tag{14}$$

The fluxes of Eq. (14) can also be written as

$$AF = -\Delta\Phi_v \tag{15}$$

where the entries of matrix A are comprised of local inverse tensor elements and $\Delta\Phi_v$ are the differences of cell edge potential differences [12] and satisfy the consistency condition that the flux is zero for constant potential.

4 HIGHER-ORDER MULTI-PHASE FLOW APPROXIMATIONS

The general finite volume discretization of Eq.(1) for multiphase flow on unstructured grids takes the form

$$(S_{p_i}^{n+1} - S_{p_i}^{n})\tau_i + \Delta t \sum_{j=1}^{N_{edV}} \mathrm{f}_p(\mathbf{S}_L^{n+q}, \mathbf{S}_R^{n+q}) F_{T_{e(i,j)}}(\phi^{n+q}) = \Delta t M_{p_i} \tag{16}$$

for the p^{th} phase continuity equation, where $\mathbf{S}_L^{n+q}, \mathbf{S}_R^{n+q}$ are the left and right hand phase saturation vectors with respect to edge $e(i,j)$ and $n+q$ denotes the time level of the scheme. Here $F_{T_{e(i,j)}} = \Lambda F_{e(i,j)}(\phi)$ and M_{p_i} denotes the p^{th} phase flow rate, prescribed at wells and is zero otherwise. The phase continuity equations are coupled through the discrete pressure equation

$$\sum_{j=1}^{N_{edV}} \Lambda(\mathbf{S}_L^{n+q}, \mathbf{S}_R^{n+q}) F_{e(i,j)}(\phi^{n+q}) = M_i \tag{17}$$

Space and space-time accurate methods are considered. The system Eq's.(16, 17) are solved semi-implicitly with a variable q $(0 < q \leq 1)$ formulation based on the Crank-Nicolson scheme in order to improve temporal accuracy [5]. The new semi-implicit CVD formulation is compared with the spatially higher order fully implicit CVD formulation with $q = 1$ presented in [3,19] in the results section.

The approximate flux is defined according to the sign of the local wave direction w_p, evaluated here at the edge mid-point. Referring to Fig. 3, with respect to a local frame of reference aligned with the direction i to k along the edge vector $\Delta\mathbf{r}_{k,i}$, the standard reservoir simulation upwind scheme is written as

$$\mathrm{f}_p(\mathbf{S}_L^{n+q}, \mathbf{S}_R^{n+q}) = \{ \begin{array}{ll} \mathrm{f}_p(\mathbf{S}_L^{n+q}) & w_p \geq 0 \\ \mathrm{f}_p(\mathbf{S}_R^{n+q}) & w_p < 0 \end{array} \tag{18}$$

and the first order upwind scheme, (known as single-point upstream weighting in the reservoir simulation literature [1]) is defined with $\mathbf{S}_L^{n+q} = \mathbf{S}_i^{n+q}$ and $\mathbf{S}_R^{n+q} = \mathbf{S}_k^{n+q}$.

4.1 Higher Order Schemes in Space

A three dimensional higher order approximation is now introduced with respect to the saturation variables. From here on it is understood that all saturations are computed at level $n+q$ depending on the choice of scheme formulation. The scheme is expressed in two-steps.

Higher order left and right hand side states are defined relative to the mid-point of each edge e (along which flux is to be defined) by expansions about the edge vertices at i and k, Fig.3. As in [3,19], the expansions are constrained with slope limiters to ensure that the higher order data satisfies a local maximum principle, preventing the introduction of spurious extrema.

First we define the difference in $\mathbf{S}$ over the edge e Fig.3, as

$$\Delta\mathbf{S}_{ki} = \mathbf{S}_k - \mathbf{S}_i \tag{19}$$

where it is now understood that $\Delta\mathbf{S}$ with a double suffix denotes a difference in $\mathbf{S}$. Referring to Fig.3 the left and right states $\mathbf{S_L}$ and $\mathbf{S_R}$ at the midpoint of the *key* edge e (joining vertices i and k) are expressed as

$$\mathbf{S_L} = \mathbf{S}_i + \frac{1}{2}\Phi^+ \Delta\mathbf{S}_{ki} \tag{20}$$

where Φ^+ is a function of

$$\mathbf{r}^+_{ki} = (\Delta\mathbf{S}_{iu}/\Delta\mathbf{S}_{ki}) \tag{21}$$

and

$$\mathbf{S_R} = \mathbf{S}_k - \frac{1}{2}\Phi^- \Delta\mathbf{S}_{ki} \tag{22}$$

where Φ^- is a function of

$$\mathbf{r}^-_{ki} = (\Delta\mathbf{S}_{dk}/\Delta\mathbf{S}_{ki}) \tag{23}$$

The differences $\Delta\mathbf{S}_{iu}$ and $\Delta\mathbf{S}_{dk}$ are well defined on a structured grid.

However extension to unstructured grids requires special construction of the differences $\Delta\mathbf{S}_{iu}$ and $\Delta\mathbf{S}_{dk}$.

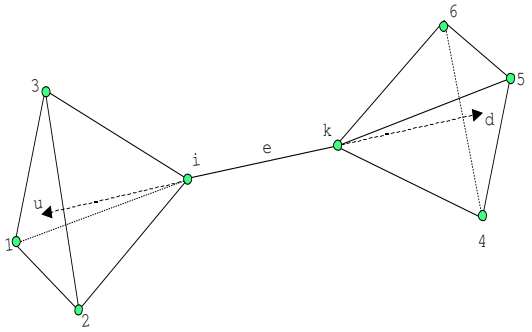

(a)

Figure 3: Higher Order Support

Directional differences are constructed by extrapolating along the *key* edge defined by vector $\Delta\mathbf{r}_{ki}$ in the respective upstream and downstream directions, see arrows in Fig.3, using the two and three dimensional procedures presented in [3,19]. The procedure is illustrated for tetrahedral cells.

Extrapolation of the respective upstream and downstream data is constrained such that a local maximum principle holds for a scalar equation. The upstream tetrahedra $i, 1, 2, 3$ is labelled T_U and the down stream tetrahedra $k, 4, 5, 6$ is labelled T_D. The space

vector corresponding to edge e ($d\mathbf{r}_{ki}$) is extrapolated into the respective tetrahedra T_U, T_D, see arrows in Fig.3. This is illustrated further with respect to vertex i. The edge vector is extrapolated to the point of intersection u, on the opposite face of the tetrahedra T_U, Fig.3. The *upwind* difference is then obtained via the expansion

$$\Delta\mathbf{S}_{iu} = \nabla\mathbf{S}_{T_U} \cdot d\mathbf{r}_{iu} \tag{24}$$

and for a linear approximation of $\mathbf{S}$ over the tetrahedra T_U the right hand side of Eq.24 is equal to the convex average of tetrahedral edge differences with

$$\Delta\mathbf{S}_{iu} = \xi_1\Delta\mathbf{S}_{i1} + \xi_2\Delta\mathbf{S}_{i2} + \xi_3\Delta\mathbf{S}_{i3} \tag{25}$$

where $\xi_i, i = 1, ...3$ are the ratio of volumes of sub-tetrahedra defined in T_U with respective sub-base areas $(u, 3, 2)$, $(u, 1, 3)$, $(u, 2, 1)$, to volume of tetrahedra T_U and are therefore positive and sum to unity. The limiter Φ^+ is defined so as to bound the higher order gradient approximation by the minimum of the slope $\Delta\mathbf{S}_{ki}$ on edge e and the slope $\Delta\mathbf{S}_{iu}$ along the extrapolated vector from i to u, with

$$\Phi^+ = \phi(r^+_{ki}) \tag{26}$$

where r^+_{ki} is defined by Eq. 21 and $\phi(r)$ is any classical slope limiter [34] and [35]. The higher order reconstruction is then bounded between $\mathbf{S}_k$ and $\mathbf{S}_u$. By convexity (Eq. 25) $\mathbf{S}_u = \xi_1\mathbf{S}_1 + \xi_2\mathbf{S}_2 + \xi_3\mathbf{S}_3$, (where $\xi_i, i = 1, ...3$ also reduce to the ratio of sub-base areas to total base area of T_U) thus bounds are such that

$$\min_{T_U \cup e}\{\mathbf{S}\} \leq \mathbf{S_L} \leq \max_{T_U \cup e}\{\mathbf{S}\} \tag{27}$$

over tetrahedra T_U and edge e yielding a local maximum principle with reconstruction reducing to first order locally at three dimensional extrema. In cases where coincidence or near coincidence is detected between the extrapolated edge and an upwind tetrahedral face or edge the limiting is collapsed to be entirely face or edge based. A similar convex average interpolant is constructed with respect to vertex k using the right hand tetrahedra T_D to obtain the difference $\Delta\mathbf{S}_{dk}$ together with analogous limiter bounds that now depend on the edge slopes $\Delta\mathbf{S}_{4k}$, $\Delta\mathbf{S}_{5k}$ and $\Delta\mathbf{S}_{6k}$ ensuring a maximum principle with $\min\{\mathbf{S}\} \leq \mathbf{S_R} \leq \max\{\mathbf{S}\}$ over T_D and edge e.

This is similar in motivation to the Local Edge Diminishing LED schemes of [36,37], with a higher order reconstruction applied to the data, (saturation field in this case). The second step of the scheme uses the upwind flux where each higher order approximation of phase saturation is upwinded via the flux using Eq's 20, 22 in Eq.18. The van-Leer (Fromm) limiter [33]

$$\phi(r) = max(0, min(2r, 2, \frac{(1+r)}{2})) \tag{28}$$

is used to define $\phi(r)$ in Eq. 27, other possible limiters are presented in [34,35]. Note as before, that the first order flux is recovered locally if the limiters are set to zero.

4.2 Higher Order Schemes in Space and Time

The system Eq's.(16, 17) are solved semi-implicitly with a variable q ($0 \leq q \leq 1$) formulation based on the Crank-Nicolson scheme in order to improve temporal accuracy in addition to spatial accuracy. While the original Crank-Nicolson scheme with $q = 1/2$ is optimal for second order time accuracy, stability and monotonicity are CFL dependent. The temporal weighting between implicit and explicit time levels is based on that presented in [5] for time accuracy, where the basic CFL (ν) stability condition is given by

$$q = max(\frac{1}{2}, 1 - \frac{1}{2\nu}) \tag{29}$$

This gives rise to a new CVD formulation which is compared below with the spatially higher order fully implicit CVD formulation with $q = 1$ presented in [3,19]. Results from the sequential scheme with $q = 0$ corresponding to implicit pressure explicit saturation (IMPES), will be presented in a future report.

5 RESULTS

The test cases involve two phase flow (oil-water) initial oil saturation is prescribed and water is injected. Water saturation contours are shown in each case. Solid wall (zero normal flow) boundary conditions are applied on all exterior boundaries of each reservoir domain. The grids employed here are fairly smooth although major changes in grid type occur. In all cases flow rate is specified at the (inflow) injector and pressure is prescribed at the (outflow) producer.

5.1 Case 1

The first case involves the classical quarter five spot problem with injection and production wells located at the lower left corner and diagonally opposite upper right corner of the domain, with triangular grid shown in Fig. 4a. The permeability tensor is assumed to be diagonal isotropic so that the pressure field is essentially Laplacian in this case, water saturation contours are shown at 0.5 pore volumes PV injected, Fig. 4. The result obtained with a consistent Darcy flux approximation and first order convective flux is shown in Fig. 4b, the result obtained with a consistent Darcy flux approximation and higher order convective flux is shown in Fig. 4c. Comparing results shows that the spatially higher order scheme provides considerable improvement in resolution of the Buckley Leverett shock front and expansion, with considerable reduction in numerical diffusion compared to the first order scheme. The results demonstrate the need for both a consistent Darcy flux approximation and higher order convective flux.

The scheme has been used with quite high CFL (above 12 at later times) with temporal errors having a strong effect on the computed solution at breakthrough. Time accuracy is tested by comparison with a solution computed by the spatially accurate scheme using a

reduced time step, by a quarter in this case Fig. 5a. This result shows further reduction in spread of the front due to the reduced temporal error, leading to later breakthrough at the producer. The result obtained using the temporally weighted scheme and original larger time step is shown in Fig. 5b. Temporal weighting is seen to be quite effective at recovering temporal accuracy, subject to a limited CFL constraint. The result at this time is computed at a global CFL up to 12, using an adapted q and time step so that q is nearer to $1/2$ than Eq. 29 would otherwise permit. However, as the rate of change in solution slows down larger CFL can be used, particularly for quasi-steady state flow.

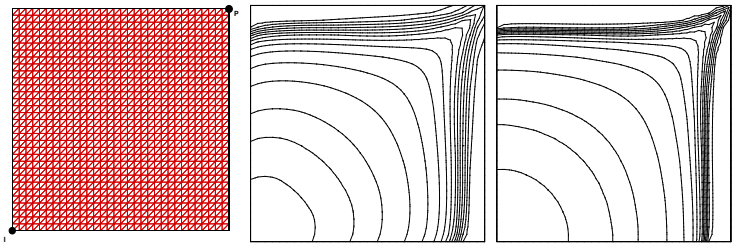

(a) (b) (c)

Figure 4: (a)Grid and Boundary Conditions, (b) CVD 1st order,(c) CVD higher order

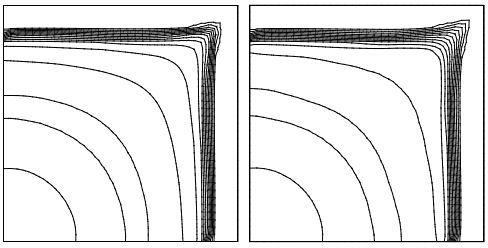

(a) (b)

Figure 5: (a) CVD higher order reduced time step, (b) CVD higher order weighted C-N

5.2 Case 2

The second case involves a three dimensional quarter five spot problem, now including gravity. Injection and production wells are located at the lower (near) left corner and diagonally opposite at the upper (far) right corner of the domain, Fig. 6. The tensor is assumed to be diagonal isotropic and the domain with varying tetrahedral grid is shown in Fig. 6. Water saturation contours are shown at 0.5 PV injected, viewed from the injector in each figure, Fig. 6. The result obtained with a consistent Darcy flux approximation and first order convective flux is shown in Fig. 6a. The contours indicate

much spreading of the Buckley Leverett front towards the producer when using a first order upwind scheme. The result obtained with a consistent Darcy flux approximation and higher order spatial convective flux is shown in Fig. 6b. The spatially higher order scheme provides considerable improvement in resolution of the Buckley Leverett shock front, and improved resolution in the effect of the lower front (not shown here) due to gravity, demonstrating the need for both a consistent Darcy flux approximation and higher order convective flux on unstructured grids in three dimensions.
This case again involves quite a high CFL (above 12 as time evolves), as a result temporal errors have a strong effect on the computed solution at breakthrough. The higher order space-time (semi-implicit scheme) result is shown in 6c and demonstrates good agreement with the reduced time-step solution (not shown here). This result shows the importance of time as well as spatial accuracy for implicit calculations.

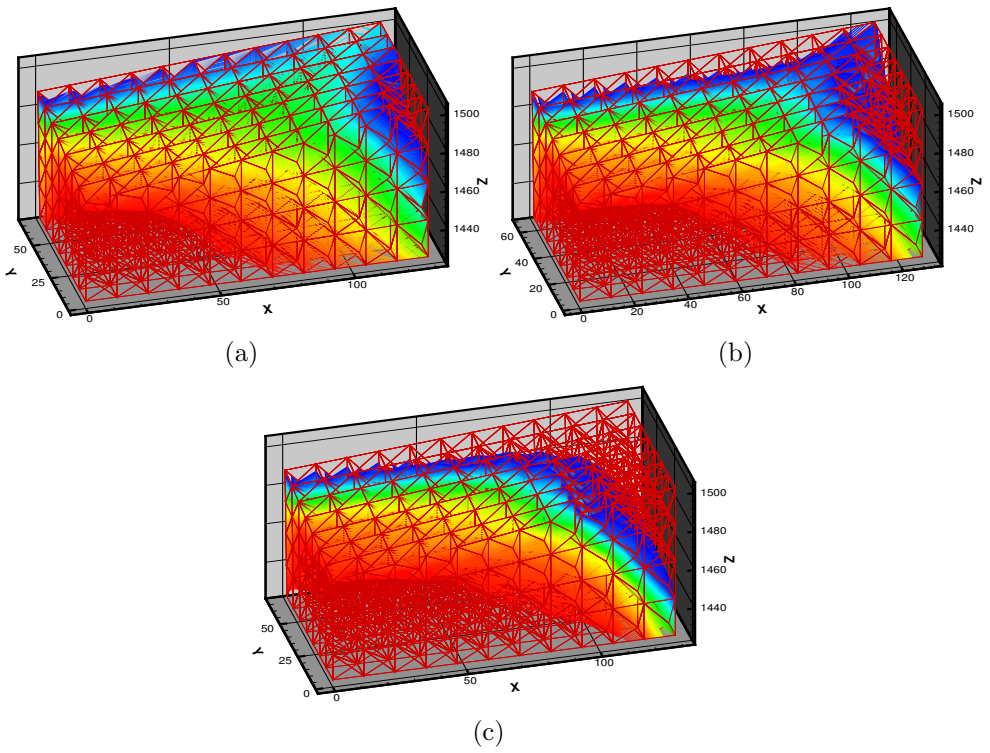

Figure 6: Tetra: Water Saturation Contours - (a) 1st Order (b) CVD higher order (c) CVD higher order weighted C-N

5.3 CVD versus CVFE

The following examples illustrates a fundamental difference in behaviour between the above CVD formulation and CVFE [32]. In contrast to the CVD schemes where flow vari-

ables and rock properties are assigned to the control-volumes, the CVFE formulation assigns flow variables to the vertices and rock properties to the cells or elements. The CVFE formulation while locally conservative, is not flux continuous across the interfaces between different cell permeability values. In general it is well known that this type of approximation can cause spreading of information when rapid changes in rock properties occur e.g. [3,19,39,40]. These examples show that while higher order fluid transport approximations can improve a low order result, higher order schemes do not compensate for the loss of information inherent in the CVFE Darcy flux.

5.4 Case 3

The geometrical domain and boundary conditions here are identical to case 2. However, a shale of 6 orders of magnitude lower permeability barrier (in bold), is now located in the middle of the domain extending approximately 2/3 across the domain from the far side, Fig.7a. The grid and snap-shot of results are viewed from the opposite side to case 2, so that the effect of the (bold) barrier can clearly be seen. The first order CVD scheme result is shown in Fig.7b. The barrier traps oil in the reservoir and the resulting saturation contours show the strong effect of the medium discontinuity. The higher order CVFE scheme result shows flow passing through the low permeability barrier, particularly near the base, which should remain essentially no-flow in regions away from the end of the barrier, Fig. 7c. In sharp contrast, the resolution of the flow in the neighbourhood of the low permeability barrier is evident in the case of the first order CVD scheme Fig. 7b, the flux-continuous CVD scheme provides much clearer resolution of flow and trapped oil near the low permeability barrier. The higher order (space-time) CVD scheme provides considerable improvement in resolution of the Buckley Leverett shock front, Fig.7d, while retaining medium discontinuity resolution.

5.5 Case 4

This test case involves three dimensional flow in a domain comprised of a mixed hybrid grid of hexahedral cells and tetrahedral cells joined by an interface comprised of a layer of pyramid cells. The domain and boundary conditions (injector lower right hand corner and producer upper left hand corner) are indicated in Fig. 8 (CVD grid). The domain is assigned a high permeability field and is divided by two low permeability barriers with drop by six orders of magnitude in permeability. The barriers are in the $(y - z)$ plane, with the second barrier placed halfway along the domain and one control-volume width (if CVD) or cell width (if CVFE) forward of the first. They extend approximately 2/3 across the domain from opposite sides 8.

The low and higher order CVD schemes are compared with the low and higher order CVFE schemes for this case at 0.75 pv injected. Only the CVD grid is shown here, Fig 8. The grids are chosen so as to approximately maintain the same problem and permeability variation with respect to the scheme formulations. Permeability is assigned

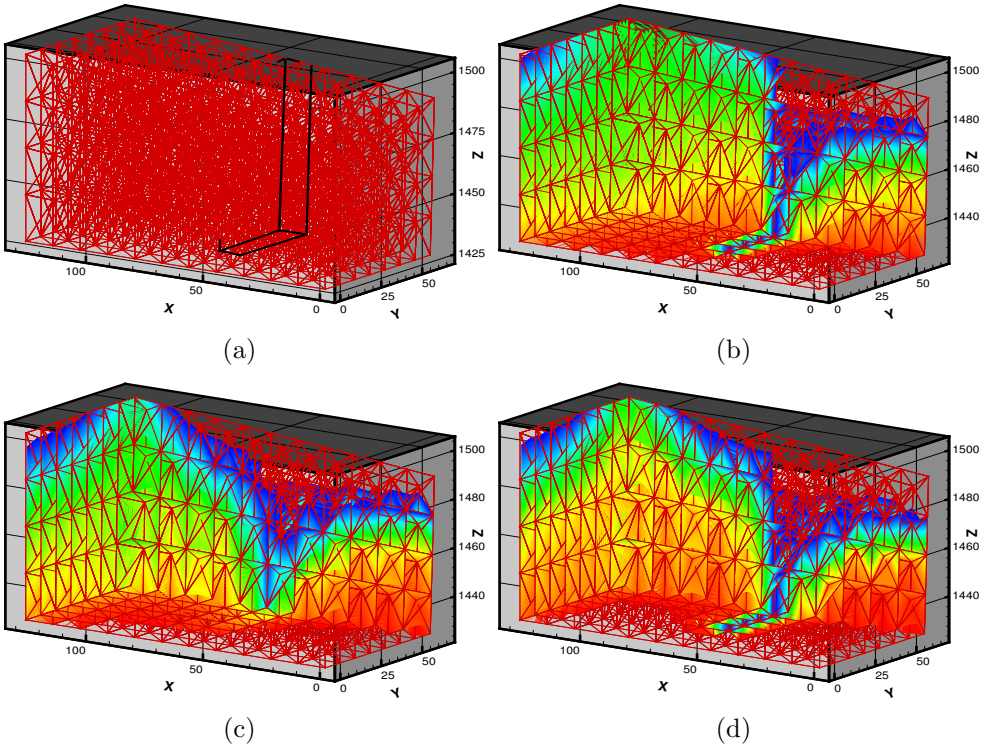

Figure 7: Tetra-barrier: Saturation Contours - (a) CVD grid and low perm-barrier (b) CVD 1st Order (c) CVFE higher order weighted C-N (d) CVD higher order weighted C-N

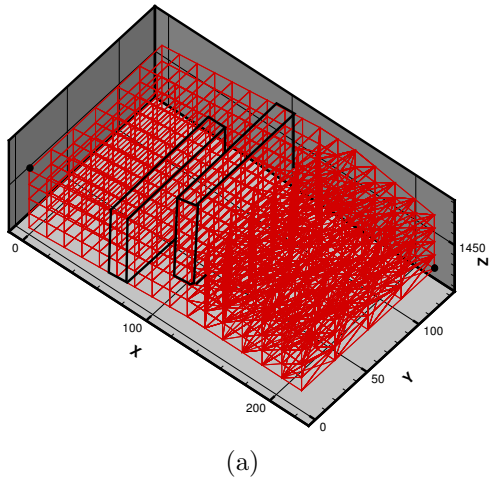

Figure 8: Hybrid Hex-Tet and pyramid layer grid with low-perm barriers CVD grid

to the control-volumes of the CVD grid and to the cells of the CVFE grid.

Results are viewed from below the domain base, where gravity is prominant. The higher order CVFE result is shown in Fig. 9a and the respective CVD result is shown in Fig. 9b. The CVFE scheme results show strong flow through the low permeability barriers, which should remain essentially no-flow in the regions away from the ends of the barriers, Fig. 9a. In sharp contrast, the resolution of flow in the neighbourhood of the low permeability barrier is evident in the case of the CVD scheme Fig. 9b, with the flux continuous CVD scheme providing much clearer resolution of flow and trapped oil near the low permeability barriers.

The higher order CVFE scheme Fig. 9a yields sharper resolution than the first order

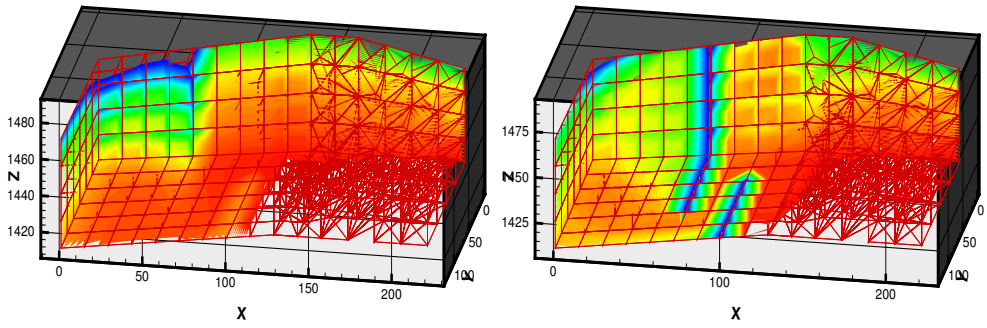

(a) (b)

Figure 9: 3D Water Saturation Contours - Hex-Tet and pyramid Layer: (a) CVFE higher order (b) CVD higher order

CVFE scheme (result not shown to save space), however the higher order scheme cannot compensate for the basically incorrect trend in flow behaviour predicted by the CVFE scheme. The averaging effect inherent in the CVFE Darcy flux approximation still induces significant flow through the low permeability barriers despite the use of a higher order convective flux. Consequently, the flow field remains quite different to that of the CVD scheme.

The higher order CVD scheme Fig. 9b provides improvement in resolution of the flow field compared to the first order CVD scheme (not shown) and the low permeability barriers are clearly detected by the higher order CVD scheme. The difference between higher order CVD (Fig. 9b) and higher order CVFE (Fig. 9a) serves to again highlight the benefits of the CVD formulation which uses the same number of degrees of freedom for flow variable approximation.

6 CONCLUSIONS

A novel higher order convective flux approximation is presented for unstructured grids in three dimensions. The resulting higher order convective flux approximations are cou-

pled with consistent and efficient continuous Darcy flux approximations. The coupling leads to new schemes for reservoir simulation on quite general structured and unstructured grids that can be comprised of tetrahedra, pyramids, prisms and hexahedra.

Benefits of the new higher order space and time CVD schemes are demonstrated by comparisons with current methods in reservoir simulation and with the standard control-volume finite element CVFE scheme which uses the same number of degrees of freedom as the new schemes.
Results are presented for two phase flow in two and three dimensions and clearly show that the higher order schemes improve front resolution. The weighted Crank-Nicolson time accurate formulations prove to be effective in improving temporal accuracy.

The CVFE scheme tends to average flow effects in the presence of rapid changes in permeability on grids of finite level. While the higher order CVFE scheme improves front resolution compared to first order CVFE, the higher order CVFE scheme cannot compensate for loss of crucial Darcy flux information that occurs as a consequence of the CVFE formulation.

In addition to improved front resolution, higher order CVD schemes significantly improve flow resolution in the presence of medium discontinuities.

7 Acknowledgements

Support of EPSRC grant GR/S70968/01 is acknowledged.

REFERENCES

[1] Aziz K. and Settari A. "Petroleum Reservoir Simulation" Applied Science Publishers, London 1979

[2] Bear J. "Dynamics of Fluids in Porous Media" American Elsevier, New York 1972

[3] Edwards M.G. Higher-Resolution Hyperbolic - Coupled - Elliptic Flux-Continuous CVD Schemes on Structured and Unstructured Grids in 2-D *to appear: International Journal for Numerical Methods in Fluids*

[4] Bell J. B. Colella P. and Trangenstein J.A. Higher Order Godunov methods for general systems of hyperbolic conservation laws. *J. Comput. Phys* 82 1989 362-397.

[5] Blunt M. J. and Rubin B. Implicit Flux-Limiting Schemes for Petroleum Reservoir Simulation. *J. Comput. Phys* 102 1992 194-210

[6] Edwards M.G. and Christie M.A. Dynamically Adaptive Godunov Schemes With Renormalization for Reservoir Simulation SPE 25268, proc: *Twelfth SPE Reservoir Simulation Symposium*, New Orleans Louisiana USA p 413-422, Feb 28-Mar 3 1993

[7] Durlofsky L.J. "A Triangle Based mixed Finite Element finite Volume Technique for Modeling Two Phase Flow through Porous Media" J Comp Phys 1993 pp 252 - 266

[8] Edwards M.G. "A Higher Order Godunov Scheme Coupled With Dynamic Local Grid Refinement for Flow In a Porous Medium" Comput. Methods. Appl. Mech. Engrg , Vol 131, pp 287 - 308, 1996

[9] Edwards M.G "Cross-Flow, Tensors and Finite Volume Approximation with Deferred Correction" Comput. Methods Appl. Mech. Engrg. 151 1998 pp 143 - 161

[10] Thiele M and Edwards M G Physically Based Higher Order Godunov Schemes for Compositional Simulation proc: *SPE Reservoir Simulation Symposium*, paper 66403 Houston TX, USA, Feb 11-14 2001

[11] Edwards M G "Non-Upwind Versus Upwind Schemes for Hyperbolic Conservation Laws in Porous Media" proc: *SPE Reservoir Simulation Symposium*, paper 93691 Houston TX, USA, 31 Jan - 2 Feb 2005.

[12] M G Edwards, "Unstructured, Control-Volume Distributed, Full-Tensor Finite Volume Schemes With Flow Based Grids , " *Computational Geosciences* , no. 6, p. 433-452, 2002.

[13] Edwards M G "Symmetric Positive Definite General Tensor Discretization Operators on Unstructured and Flow Based Grids" proc: ECMOR VIII *8th European Conference on the Mathematics of Oil Recovery*, Frieberg Germany Sept 3-6th 2002

[14] Edwards M G Control-volume distributed sub-cell flux schemes for unstructured and flow based grids. *SPE Reservoir Simulation Symposium, Houston, Texas, USA, 3-5 Febuary 2003.*

[15] Edwards M. G. "Split Full Tensor Discretization Operators for Structured and Unstructured Grids in Three Dimensions" SPE 66358 proc: SPE Reservoir Simulation Symposium Houston, Texas, 11-14 February 2001.

[16] Edwards M. G. "M-matrix Flux Splitting for General Full Tensor Discretization Operators on Structured and Unstructured Grids" J. Comput. Phys 160, pp 1-28, 2000

[17] Edwards M. G. "Simulation With a Full-Tensor Coefficient Velocity Field Recovered From a Diagonal Tensor Solution" SPE Journal 5 2000, 387-393

[18] Edwards M.G. and Rogers C.F "Finite Volume Discretization with Imposed Flux Continuity for the General Tensor Pressure Equation " Computational Geosciences vol 2 1998, pp 259 - 290.

[19] Edwards M.G. Higher-Resolution Hyperbolic - Coupled - Elliptic Flux-Continuous CVD Schemes on Structured and Unstructured Grids in 3-D *to appear: International Journal for Numerical Methods in Fluids*

[20] Aavatsmark I. *Introduction to multipoint flux approximation for quadrilateral grids.* Comput.Geo(2002),no.6,405-432.

[21] Aavatsmark I. , T. Barkve, and T. Mannseth. "Control-Volume Discretization Methods for 3D Quadrilateral Grids in Inhomogeneous, Anisotropic Reservoirs" SPE Reservoir Simulation Symposium, Dallas TX USA, 1997

[22] Aavatsmark I., T. Barkve, Ø. B*øe* and T. Mannseth, "Discretization on Unstructured Grids for Inhomogeneous, Anisotropic Media" Part 1 Methods SIAM J Sci. Comput. 19, (1998), 1700-1716

[23] Aavatsmark I., T. Barkve, Ø. B*øe* and T. Mannseth, "Discretization on Unstructured Grids for Inhomogeneous, Anisotropic Media" Part II Results SIAM J Sci. Comput. 19 (1998), 1717-1736

[24] Verma S. and Aziz K. "A Control Volume Scheme for Flexible Grids in Reservoir Simulation" SPE 37999 14th SPE Reservoir Simulation Symposium, Dallas, Texas, USA, pp 215, 227, 8-11 June 1997

[25] Lee S. H. Durlofsky L. J. Lough M. F. and Chen W. "Finite Difference Simulation of Geologically Complex Reservoirs With Tensor Permeabilities. SPE 38002 1997, SPE Reservoir Simulation Symposium, Dallas TX USA

[26] Lee S. H., Tchelepi H. and DeChant L. J. "Implementation of a Flux Continuous Finite Difference Method for Stratigraphic Hexahedron Grids" paper SPE 51901 proc: SPE Reservoir Simulation Symposium, Houston, Texas, USA Feb 14th - 17th 1999

[27] Arbogast T., Wheeler M. F. and I. Yotov "Mixed Finite Elements for Elliptic Problems with Tensor Coefficients as Cell centered Finite Differences" SIAM J. Numer. Anal. 34(2), 828 1997

[28] Raviart R. A. and Thomas J. M. "A Mixed Finite Element method for Second Order Problems" Lecture Notes in Mathematics 606, Springer-Verlag New York 1977 pp 292 - 315

[29] Russel T. F. and Wheeler M. F. "Finite Element and Finite Difference Methods for Continuous Flows in Porous Media". Chapt 2, in the Mathematics of Reservoir Simulation, R.E. Ewing ed, Frontiers in Applied Mathematics SIAM 1983, pp 35 -106

[30] Farmer C. L. , D. E. Heath and R. O. Moody "A Global Optimization Approach to Grid Generation" 11th SPE Reservoir Simulation Symposium, Anaheim CA, USA 17-20 Feb 1991 pp 341-350

[31] Russell T.F. *Relationships among some conservative discretization methods, in: Numerical Treat ment of Multiphase Flows in Porous Media*, eds. Z. Chen et al., Lecture Notes in Physics, Vol. 552 (Springer, Heidelberg, 2000) pp. 267–282.

[32] Forsyth P. "A Control-Volume Finite Element Method for Local Mesh Refinement in Thermal Reservoir Simulation" SPERE Nov 1990 p 561

[33] Godlewski E. and Raviart P. Numerical Approximation of Hyperbolic Systems of Conservation Laws App. Math. Sci. 118 Springer-Verlag, New York. 1996

[34] van Leer B. Towards the ultimate Conservative Difference Scheme V. A Sequel to Godunov's Method *J. Comput. Phys*, 32:101-136, 1979

[35] Sweby P. High Resolution Schemes Using Flux Limiters for Hyperbolic Conservation Laws. SIAM J. Numer. Anal., 21,995-1011, 1984.

[36] Jameson A. Artificial Diffusion, Upwind Biasing, Limiters and Their Effect on Accuracy and Multigrid Convergence in Transonic and hypersonic Flows. AIAA 93-3359 1993

[37] Lyra P and Morgan K. A Review and Comparative Study of Upwind Biased Schemes for Compressible Flow Computation Part III: Multidimensional Extension on Unstructured Grids *Arch. Comput. Meth. Engng.* vol 9, 3,207-256 2002

[38] Shu C. W. and Osher S. Efficient Implementation of Essentially Non-Oscillatory Shock Capturing Schemes *J. Comput. Phys*, 77:439-471 1988.

[39] Prevost M, Edwards M G and Blunt M J Streamline Tracing on Cuvilinear Structured and Unstructured Grids *SPE Journal* June 2002

[40] Klausen R and Eigstad G Multipoint Flux Approxiamtions and Finite Element Methods; Practical Aspects of Discontinuous Media ECMOR VIII proc: *9th European Conference on the Mathematics of Oil Recovery* Cannes, France 30th Aug-2nd Sept 2004

[41] Pal M, Edwards M G and Lamb A. R. Convergence Study of a Family of Flux-Continuous, Finite Schemes for the General Tensor Pressure Equation *to appear: International Journal for Numerical Methods in Fluids*

[42] Pal M, Edwards M G Family of Flux-continuous Finite-volume Schemes with Improved Monotonicity and Convergence ECMOR X proc: *10th European Conference on the Mathematics of Oil Recovery* Amsterdam, The Netherlands 4-7th Sept 2006